# Stacking patterns and carrier mobilities of GeS bilayer

**Fazel Shojaei[1], Hong Seok Kang[2]***

[1]Department of Chemistry and Bioactive Material Sciences and Research Institute of Physics and Chemistry, Jeonbuk National University, Jeonju, Chonbuk 561-756, Republic of Korea
[2]Department of Nano and Advanced Materials, College of Engineering, Jeonju University, Hyoja-dong, Wansan-ku, Chonju, Chonbuk 560-759, Republic of Korea

*Corresponding author

## Abstract

Based on the first-principles calculations, we identify four stacking patterns of the GeS bilayer, in which two most stable ones are almost equally stable. The most stable one corresponds to the experimental pattern in bulk GeS. Its interlayer binding is stronger than those in $\alpha$-phosphorene and graphene, indicating that the material will rather exist in the form of bilayers or multilayers. Our HSE06 band structure calculations show that both patterns are semiconductors with indirect band gaps in the visible region, which are slightly smaller than that of the monolayer. For the monolayer, our refined calculation based on the deformation potential approximation indicates that the electron mobility along the armchair direction amounts to $4.62 \times 10^4$ cm$^2$ V$^{-1}$s$^{-1}$, which is ~40 times larger than that of the $\alpha$-phosphorene. The electron mobility of the bilayer is dependent on the stacking pattern. The most stable pattern is expected to exhibit the mobility of $1.69 \times 10^4$ cm$^2$V$^{-1}$s$^{-1}$, which is still ~30 times larger than that of the bilayer $\alpha$-phosphorene. A detailed comparison of the carrier mobilities suggests that both of the mono- and bi-layer will be useful for *n*-type electronics. Copyright © 2018 VBRI Press.

**Keywords:** First-principles calculation, bilayer formation, band gap, stacking pattern, deformation potential method, carrier mobility.

## Introduction

Recently, extensive attention has been paid to two-dimensional (2D) materials which can be used in nanoelectronics for post-silicon era. For this purpose, the materials should not only exhibit high carrier mobilities but also have sizeable band gaps. Black ($\alpha$) phosphorene is under very active study, since it has been exfoliated from black phosphorus into fewlayers [1,2]. Since their layers are held together by weak van der Waals interactions, their electronic and physical properties are largely determined by quantum confinement effect and possible anisotropy in the chemical structures along two in-plane directions [3].

Group IV monochalcogenides share the same ground-state orthorhombic crystal structure with black phosphorus. Anisotropic chemical structures account for anisotropy in electrical and thermal conductivities [4,5]. For GeS, GeSe, SnS, and SnSe, coupled ferroelectricity and ferroelasticity were theoretically predicted at room temperature, which may have applications in nonvolatile memory [6]. Structural phase transitions were also predicted for monolayers and bilayers of GeSe and SnSe at a critical temperature below the melting temperature [7]. Experimentally, bulk SnS was applied to solar cells [8]. Thin nanodisks of SnSe and SnSe$_2$ synthesized based

on a one-pot chemical route showed excellent specific capacitance for supercapacitors [9]. A surprising record of ZT ≈ 2.6 was reported in *p*-type SnSe single crystal, which represents dimensionless thermoelectric figure of merit [10]. The same crystal also exhibited ZT ≈ 2.2 when it becomes *n*-type by doping bismuth [11]. Freestanding monolayers of SnS and SnSe were recently exfoliated [12]. They were shown to exhibit 67.1% of photon-to-current conversion efficiency (IPCE), strikingly higher than the 1.66 efficiency of its bulk counterpart. Interestingly, Sn-sulfides and Sn-selenides also exist in hexagonal phase when they form dichalcogenides [13]. Contrary to the case of their monochalcogenides, their bulk phases are *n*-type [14,15].

Germanium monochalcogenides are particularly interesting because their bulk have band gaps that overlap well with the solar spectrum. Optical measurements indicates that their bulk have indirect gaps of 1.58 and 1.14 eV for bulk GeS and GeSe, respectively [16]. Their monolayers exhibit the largest band gaps among all group IV monochalcogenides [17]. Specifically, a calculation predicts that GeS monolayer will show much stronger anisotropy in thermal conductivity than SnS and SnSe monolayers [18]. Another calculation indicates that GeS monolayer can be a quite promising catalyst for oxygen

evolution reaction due to its considerably low overpotential [**19**]. Energy barrier for Li diffusion along zigzag direction of GeS monolayer is also smaller than those of other 2D materials [**20**]. In this work, we will first shows that the GeS will exist in the form of bilayers or multilayers rather than as monolayers when exfoliated. This observation motivates us to further investigate carrier mobilities of the bilayer, finding that it can be promising for *n*-type electronics because its electron mobility will be much larger than that of the bilayer α-phosphorene.

## Theoretical methods

Geometry optimizations were performed using the Vienna ab-initio simulation package (VASP) [**21,22**]. The electron-ion interactions were described using the projector-augmented wave (PAW) method, which is primarily a frozen-core all-electron calculation [**23**]. Attractive van der Waals interactions were taken into account employing Grimme's D2 correction method for the PBE exchange-correlation functional [**24**]. For structure optimization, atoms were relaxed in the direction of the Hellmann-Feynman force using the conjugate gradient method with an energy cut-off of 500 eV until a stringent convergence criterion (<0.001 eV/Å) was satisfied.

HSE06 hybrid functional was employed for accurate electronic structure calculations [**25**]. We maintained a sufficiently large vacuum space of 15 Å along the direction normal to the monolayer plane so that there were no appreciable interactions between two adjacent supercells. We defined the X and Y axes to be parallel to the longer (*a*) and shorter (*b*) dimensions of the rectangular primitive cell of the monolayer, respectively. The *k*-point sampling was performed using Γ-centered *k*-point meshes of 16×14×1 for geometry optimizations and 10×8×1 for electronic structure calculations.

In a 2D system, the carrier mobility can be calculated from the deformation potential (DP) approximation:[**26**]

$$\mu_{2D} = \frac{e\hbar^3 C_{2D}}{kT m^* m_d (E_1^i)^2} \quad (1)$$

where $C_{2D}$ is the elastic modulus of the longitudinal strain in the transport direction, $m^*$ is the effective mass of the carrier in the same direction, $m_d$ is the average effective mass in the two directions given by $m_d = \sqrt{m_x^* m_y^*}$ and $E_1^i$ mimics the deformation energy constant of the carrier due to phonons for the *i*-th edge band along the transport direction through the relation: $E_1^i = \Delta E_i / (\Delta l / l_0)$, where $\Delta E_i$ and $\Delta l / l_0$ represent the energy change of the *i*-th band and lattice dilation, respectively.
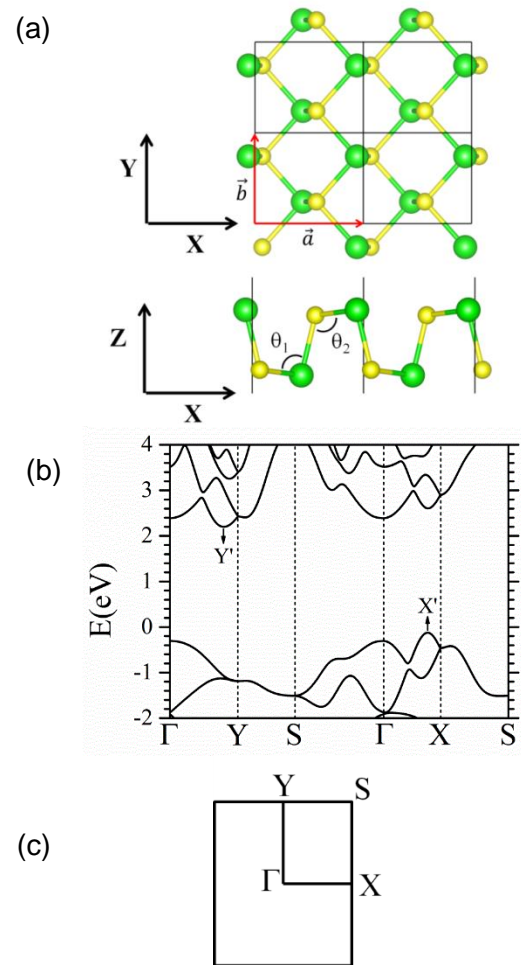


**Fig. 1.** The chemical structure (a) and HSE06 band structure (b) of the α-GeS monolayer. Its first Brillouin zone is also shown in (c), where points of spatial symmetry are labelled. For better understanding, two primitive cells are shown, where two primitive vectors ($\vec{a}$, $\vec{b}$) as well as two bond angles (θ₁ and θ₂) are also defined. Green and yellow colors represent germanium (Ge) and sulfur (S) atoms, respectively.

## Results and discussion

A GeS monolayer consists of germanium (Ge) and sulfur (S) atoms in a puckered honeycomb structure in such a way that each germanium atom is bonded to three neighboring sulfur atoms and vice versa. We name it α-GeS, since its structure resembles that of well-known α-phosphorene (α-P). As shown in **Fig. 1 (a)**, α-GeS has a rectangular primitive cell with two Ge and two S atoms. Its optimized lattice constants along the armchair and zigzag directions are *a* = 4.44 Å and *b* = 3.65 Å, respectively. These values are in good agreement with previous calculations for the monolayer [17,27-29] and the experimental values (4.30, 3.65) of its multilayer [16,30]. When compared with the case of α-P, the *a* constant is about 3% shorter, which is due to much smaller puckering angles along the armchair direction. Specifically, the θ₁ angles (= 93.9°) around Ge atoms in **Fig. 1(a)** are appreciably smaller than the corresponding P-P-P angles (= 103.9°) in the α-P, while the θ₂ angle (= 103.7°) around S atoms are only slightly smaller.

On the one hand, the *b* constant is about 10% longer, which can be attributed to longer Ge-S bonds (= 2.48 Å) than the zigzag P-P bonds in the α-P (2.22 Å) [31].

In consistency with previous calculations, **Fig. 1 (b)** shows that the HSE06 band structure indicates that the α-GeS monolayer is semiconducting with an indirect band gap of 2.31 eV for X'→ Y' transitions [17,27-29]. Here, X' and Y' denote *k*-points corresponding to the valance band maximum (VBM) and conduction band minimum (CBM) located at 75% along Γ→X and Γ→Y paths, respectively. The gap is significantly larger than that (= 1.65 eV for the Γ→Γ) of the monolayer α-P [31]. The difference (ΔE$_g$ = 0.38 eV) between the direct gap at Γ point and the indirect gap is appreciable. The second VBM, i.e., VB(Γ), occurs at the Γ point, whose energy eigenvalue is only 0.18 eV lower than that at the X'. We recall that the corresponding difference (= -0.08 eV) in the α-AsP is even smaller [31]. Similar to the case in the α-AsP, the VBM(X') and VB(Γ) represent in-plane $p_x$- and out-of-plane $p_z$-states, respectively [See Figures S1(a) and S1(b) for their charge density distributions]. On the one hand, the CBM(Y') and CB(Γ) also represent in-plane $p_y$-states and out-of-plane $p_z$-states, respectively. [See Figures S2(a) and S2(b) for their charge density distributions].

Now, we use the DP approximation to calculate carrier mobilities in the α-GeS monolayer at 300 K. **Table 1** summarizes various parameters involved in the calculation, i.e., the effective mass ($m_e^*$, $m_h^*$) of electrons and holes, the elastic modulus ($C_{2D}^{armchiar}$, $C_{2D}^{zigzag}$), and the deformation energy (E$_1^{VBM}$, E$_1^{CBM}$). As in the case of the α-P, all these parameters are largely different along the armchair and zigzag directions, implying anisotropic electron and hole mobilities ($\mu_e$, $\mu_h$) [3]. Specifically, E$_1^{CBM}$ along the armchair direction (= 0.33 eV) is appreciably smaller than that (= 3.63 eV) along the zigzag direction, being directly responsible for a highly anisotropic electron mobilities, i.e., $4.62\times10^4$ and $0.52\times10^3$ cm$^2$ V$^{-1}$s$^{-1}$ along the two directions. Our E$_1^{CBM}$ is about 4 times smaller along the armchair direction than Li

et al.'s datum [28]. As Figures S3(a) and S3(b) show, almost linear variations of the band edge positions with the lattice dilation clearly demonstrate the reliability of our procedure.

For the CBM, the smaller deformation energy along the armchair direction can be explained by its charge density distribution shown in Figure S2(a). The in-plane interaction along the armchair direction is much less sensitive to the lattice dilation than that along the other direction. On the one hand, the hole mobilities (= $8.00\times10^1$ and $3.10\times10^2$ cm$^2$V$^{-1}$s$^{-1}$ along the armchair and zigzag directions, respectively) are more than two order of magnitudes smaller than the electron mobility, revealing that the monolayer will be more useful in *n*-type electronics. We recall that the electron mobility is about 40 times larger than that of the α-P [3].
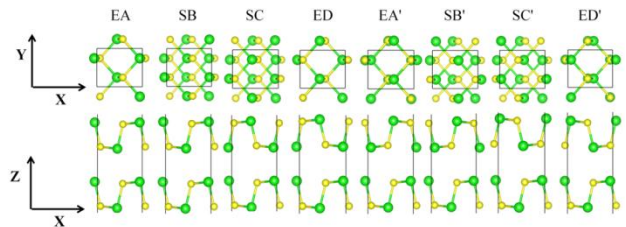


**Fig. 2** Eight initial stacking patterns of the α-GeS bilayer in two different views. Green and yellow colors represent germanium (Ge) and sulfur (S) atoms, respectively.

Knowing that geometric and electronic properties of 2D layered materials are thickness-dependent, a question arises: how do the band gap and carrier mobilities change when two α-GeS monolayers are stacked to form a bilayer? To address this question, we first investigate eight different initial stacking patterns of the bilayer shown in **Fig. 2**: EA, SB, SC, ED, EA', SB', SC', and ED'. When viewed along the Z direction, two layers are eclipsed in EA, EA', ED, and ED', while they are staggered in SB, SB', SC, and SC'. In EA, the upper layer is directly stacked on top of the lower layer. SB, SC, and ED can be generated from EA by translating its upper layer by (0, 1/2), (1/2, 0), and (1/2, 1/2), respectively. EA',

**Table 1**. Elastic modulus ($C_{2D}$), effective mass ($m_e^*$, $m_h^*$) of electrons and holes with respect to a free-electron mass ($m_0$), the deformation energy of the CBM and VBM ($E_1^{CBM}$, $E_1^{VBM}$), and the mobility ($\mu_e$, $\mu_h$) of electrons and holes along two directions (zigzag and armchair) for the α-GeS monolayer (N$_L$ = 1) as well as those for the two most stable stacking patterns of the α-GeS bilayer (N$_L$ = 2). For each system, the modulus is calculated using the PBE-D2 functional, while the effective mass and the deformation energy are calculated using the HSE06 functional.

| N$_L$ | | Direction | $C_{2D}$ (J/m²) | Electron | | | Hole | | |
|---|---|---|---|---|---|---|---|---|---|
| | | | | $m_e^*$ | $E_1^{CBM}$(eV) | $\mu_e$[b] | $m_h^*$ | $E_1^{VBM}$(eV) | $\mu_h$[b] |
| 1 | α-GeS[a] | Zigzag | 52.27(50.98) | 0.49(0.41) | 3.63±0.02 (1.73) | 0.52-0.53 (2.95) | 0.41(0.61) | 5.33±0.04 (9.32) | 0.31-0.32 (0.05) |
| | | Armchair | 17.40(15.29) | 0.22(0.20) | 0.33±0.01 (1.19) | 43.05-49.72 (3.68) | 0.22(0.23) | 8.15±0.12 (4.85) | 0.08-0.09 (0.16) |
| 2 | SB' | Zigzag | 105.84 | 0.36 | 3.32±0.03 | 1.82-1.89 | 0.55 | 7.96±0.00 | 0.13 |
| | | Armchair | 35.38 | 0.26 | 0.75±0.02 | 16.46-17.65 | 0.43 | 7.00±0.03 | 0.07 |
| | SB | Zigzag | 100.01 | 1.56 | 5.09±0.02 | 0.05 | 0.63 | 6.00±0.03 | 0.2 |
| | | Armchair | 32.39 | 0.83 | 2.42±0.03 | 0.12-0.13 | 0.34 | 7.76±0.04 | 0.07 |

[a]Values inside parenthesis denote those reported in Ref. 28.

[b]Mobility at 300 K in units of $10^3$ cm$^2$ V$^{-1}$s$^{-1}$.

SB', SC', and ED' can be built from EA, SB, SC, and ED by rotating the upper layer by 180° with respect to the Z axis, respectively. We find that eclipsed patterns transform into staggered ones after optimization. In fact, EA, ED, EA', and ED' relax to SB, SC, SB', SC', respectively, while four staggered patterns keep their initial structures.

**Table 2** summarizes various parameters for the staggered patterns of the α-GeS bilayer. Our PBE-D2 calculations show that SB' is the most stable configuration, being 3, 11, and 13 meV/atom more stable than the SB, SC, and SC', respectively. This pattern corresponds to the experimental one in the bulk and multilayer α-GeS [16,30]. The small energy difference between the SB and SB' indicates that the former one can be easily generated by stacking fault. The table also shows that relative stabilities of various patterns generally correlate with interlayer distance. It is the smallest in pattern SB' (= 2.73 Å), being slightly smaller than the experimentally observed value (2.78 Å) for the multilayer α-GeS [30]. In addition, the interlayer binding energies (= 61 and 58 meV/atom for patterns SB' and SB, respectively) of the two most stable patterns are larger than that of the bilayer α-P (= 39 meV/atom). They are also appreciably larger than that of the bilayer graphene (= 26 meV/atom) calculated in this work. Therefore, we can expect that the α-GeS bilayer will exists in the form of bilayers or multilayers rather than in the form of monolayers. From now on, we will limit our further discussions on the two most stable patterns of the bilayer, i.e, SB' and SB.

Here, we focus on the electronic properties of the bilayer. As **Fig. 3(a) and Table 2** show, SB' exhibits an indirect band gap of 2.08 eV for X'→Y' transition, which is 0.24 eV lower than that of the monolayer for the same transition. The energy difference between the direct gap at the Γ-point and the indirect one ($\Delta E_g$ = 0.20 eV) becomes smaller than the corresponding value (= 0.38 eV) for the monolayer. The VB at the Γ point corresponds to an antibonding interaction of $p_z$ states belonging to different layers. It is destabilized to a certain extent, because the smallest interlayer Ge-Ge (3.45 Å) and S-S (3.66 Å) distances allow appreciable interaction between them. On the one hand, the VB(X') corresponds to an antibonding interaction between two $p_x$ states, which are less altered by the interaction. This is the reason why the energy difference of the VB at X' and Γ points decreases. Recall that the CBM(Y') and CB(Γ) of the monolayer represent in-plane $p_y$-states and out-of-plane $p_z$-states, respectively. Therefore, we can easily understand that the bonding interaction of the CB will be appreciable at the Γ point. Although the interaction apparently seems to be negligible at the Y'-point, the specific geometry of the pattern still allows an appreciable interaction between them in a way which is not possible in the case of the VB(X'). Consequently, both of CB(Γ) and CB(Y') are stabilized by nearly the same amount, still leaving the CBM at the Y' point.

Meanwhile, **Fig. 3(b)** and **Table 2** show that SB configuration still displays an indirect gap of 2.17 eV for

the X'→Γ transition, which is comparable to that of SB'. Its band structure is almost similar to that of SB'. However, there are two major differences between them. First, the CBM of SB occurs at the Γ point instead of Y'. Second, the direct gap is almost comparable to the indirect one, as indicated by its smaller value of $\Delta E_g$ (= 0.07 eV). Different from the case of SB' aforementioned, the geometry does not allow stabilization of the CB at the Y'-point. Hence, the CBM occurs at the Γ point.

**Table 2.** Various parameters for various stacking patterns of the α-GeS bilayer.

| Pattern | $E_{rel}$ (eV/atom)[a] | $a,b$(Å)[b] | $E_L$ (eV/atom)[c] | $d_L$ (Å)[d] | $l_{Ge-S}$ (Å)[e] | $E_g^d$ (eV)[f] | $E_g^{in}$ (eV)[g] | $\Delta E_g$(eV)[h] |
|---|---|---|---|---|---|---|---|---|
| SB' | 0.000 | 4.40,3.65 | 0.061 | 2.73 | 2.42,2.46 | 2.28(Γ→Γ) | 2.08 (X'→Y') | 0.20 |
| SB | 0.003 | 4.36,3.67 | 0.058 | 2.80 | 2.43,2.47 | 2.24 (Γ→Γ) | 2.17 (Y'→ Γ) | 0.07 |
| SC | 0.011 | 4.25,3.71 | 0.050 | 2.96 | 2.41,2.48 | - | - | - |
| SC' | 0.013 | 4.34,3.67 | 0.048 | 2.93 | 2.42,2.48 | - | - | - |

[a]The relative stability the pattern of with respect to SB'.
[b]PBE-D2-optimized lattice constants.
[c]The interlayer binding energy per atom.
[d]The interlayer distance, which is defined as the difference between the maximum and minimum Z coordinates of the lower and upper layers, respectively.
[e]The intralayer Ge-S bond length. Two values correspond to the out of plane and in-plane Ge-S bonds lengths, respectively.
[f]The direct band gap obtained from the HSE06 calculation. The *k*-points for the transition are also shown in the parenthesis.
[g]The indirect band gap obtained from the HSE06 calculation. The *k*-points for the transition are also shown in the parenthesis.
[h]The energy difference between direct and indirect gaps defined as $\Delta E_g$ = $E_g^d$ - $E_g^{in}$.
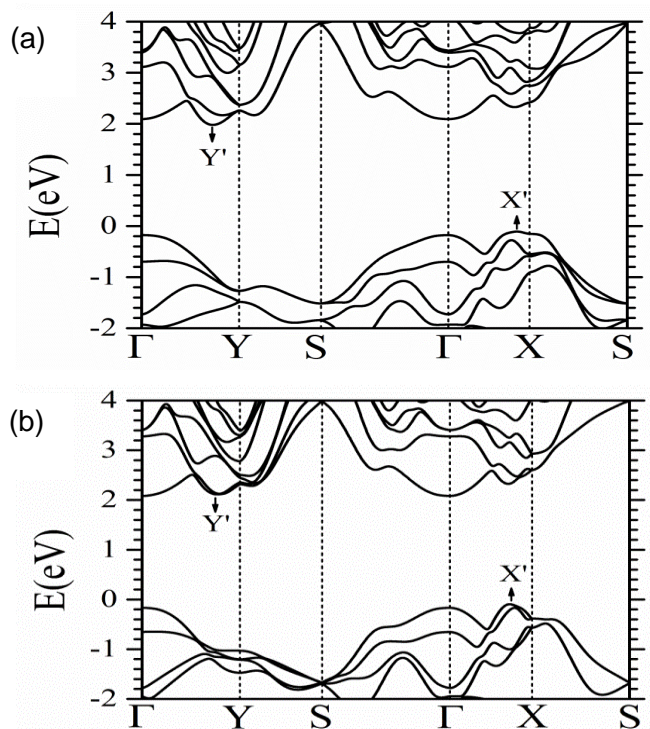


**Fig. 3.** The HSE06 band structure of the bilayer α-GeS in patterns SB' (a) and SB (b).

Now we turn our attention to the carrier mobility of the bilayer shown in **Table 1**. In each of the two stacking patterns, the $C_{2D}$ parameter is approximately twice of that of the monolayer irrespective of direction. The $m_e^*$ and $m_h^*$ values are generally not highly sensitive to the bilayer formation. However, $m_e^*$ values are ~4 times larger than those of the monolayer along the two directions in pattern SB, which can be ascribed to the change of the $k$-point for the CBM. The $E_1^{VBM}$ values of both patterns are slightly different from those of the monolayer, resulting in no appreciable change in the hole mobilities after the bilayer formation.

Estimated electron mobilities of SB' and SB along the armchair direction are $1.69 \times 10^4$ and $1.2 \times 10^2$ cm$^2$V$^{-1}$s$^{-1}$, respectively, being ~3 and ~375 times smaller than that of its monolayer. This is because the bilayer formation increases the $E_1^{CBM}$ value along the direction, particularly for SB. This observation can be understood by comparing the charge density distribution of the CBM in the two patterns. We recall that the CBM occurs at Y' and $\Gamma$ points for SB' and SB, respectively. As can be compared in Figures S4(a) and 4(b), the energy eigenvalue of the CBM in the SB will be more sensitive to the dilation along the armchair direction, because the state represents appreciable interaction along the direction. In SB', the electron mobility is still anisotropic, being higher along the armchair direction. In fact, its electron mobility is about 28 times larger than that of the bilayer $\alpha$-P [3]. On the other hand, its hole mobility ($1.3 \times 10^2$ cm$^2$V$^{-1}$s$^{-1}$) is about two orders of magnitudes smaller than the electron mobility ($1.69 \times 10^4$ cm$^2$V$^{-1}$s$^{-1}$). Therefore, the bilayer will be still useful as an $n$-type material in the most stable pattern, if we take into account that the stacking fault in SB will deteriorate the mobility.

## Conclusion

First, we have identified four stacking patterns of the GeS bilayer, in which two most stable ones (SB' and SB) are almost equally stable. The most stable one (SB') corresponds to the experimental pattern in bulk GeS. Its interlayer binding is stronger than those in $\alpha$-phosphorene and graphene, indicating that it can be more difficult to exfoliate into monolayers. Our HSE06 band structure calculations have shown that both patterns are semiconductors with indirect band gaps in the visible region (= 2.08 and 2.17 eV for the two patterns), which are slightly smaller than that of its monolayer. We have also calculated carrier mobilities of the mono- and bilayers using the deformation potential approximation. For the monolayer, our refined calculation have indicated that the electron mobility along the armchair direction amounts to $4.62 \times 10^4$ cm$^2$ V$^{-1}$s$^{-1}$, which is ~40 times larger than that of the $\alpha$-P. On the other hand, its hole mobility is more than two order of magnitudes smaller along either direction, suggesting that the monolayer will be useful for $n$-type electronics. The electron mobility of the bilayer is found to be dependent on the stacking pattern, and the most stable pattern (SB') is expected to display the

mobility of $1.69 \times 10^4$ cm$^2$V$^{-1}$s$^{-1}$, which is smaller than that of its monolayer but ~30 times larger than that of the bilayer $\alpha$-P. Therefore, we can expect that the bilayer will be still useful for $n$-type electronics.

**Supporting information**

Supporting informations are available from VBRI Press.

The charge density distribution of the VB for the $\alpha$-GeS monolayer (Figure S1), the charge density distribution of the CB for the $\alpha$-GeS monolayer (Figure S2), energy eigenvalues of the band edge positions of the $\alpha$-GeS monolayer as functions of the lattice dilation (Figure S3), and the charge density distribution of the CBM for patterns SB' and SB of the $\alpha$-GeS bilayer (Figure S4).

**References**

1. Liu, H.; Neal, A. T.; Zhu, Z.; Luo, Z.; Xu, X.; Tomanek, D.; Ye, D.; *ACS Nano*, **2014**, *8*, 4033.
   **DOI:** 10.1021/nn501226z
2. Woomer, A. H.; Farnsworth, T. W.; Hu, J.; Wells, R. A.; Donley, C. L.; Warren, S. C.; *ACS Nano*, **2015**, *9*, 8869.
   **DOI:** 10.1021/acsnano.5b02599
3. Qiao, J.; Kong, X.; Hu, Z.-X.; Yang, F.; Ji, W.; *Nature Comm.*, **2014**, *5*, 4475.
   **DOI:** 10.1038/ncomms5475
4. Shi, G.; Kioupakis; E.; *Nano Lett.*, **2015**, *15*, 6926.
   **DOI:** 10.1021/acs.nanolett.5b02861
5. Li, C. W.; Hong, J.; May, A. F.;Bansal, D.; Chi, S.; Hong, T.; Ehlers, G.; Delaire, O.; *Nat. Phys.*, **2015**, *11*, 1063.
   **DOI:** 10.1038/nphys3492
6. Wu, M.; Zeng, X. C.; *Nano Lett.*, **2016**, *16*, 3236.
   **DOI:** 10.1021/acs.nanolett.6b00726
7. Mehrshad, M.; Fregoso, B. M.; Yang, Y.; Zhu, W.; van der Zande, A.; Ferrer, J.; Bellaiche, L.; Kumar, P.; Barraza-Lopez, S.; *Phys. Rev. Lett.*, **2016**, *117*, 246802.
   **DOI:** 10.1103/PhysRevLett.117.246802
8. Steinmann, V.; Jaramillo, R.; Hartman, K.; Chakraborty, R.; Brandt, R. E.; Poindexter, J. R.; Lee, Y. S.; Sun, L.; Polizzotti, A.; Park, H. H.; Gordon, R. G.; Buonassisi, T.; *Adv. Mater.*, **2014**, *26*, 7488.
   **DOI:** 10.1002/adma.201402219
9. Zhang, C.; Yin, H.; Han, M.; Dai, Z.; Pan, H.; Zheng, Y.; Lan, Y.-Q.; Bao, J.; Zhu, J.; *ACS Nano*, **2014**, *8*, 3761.
   **DOI:** 10.1021/nn5004315
10. Zhao, L.-D.; Lo, S.-H.; Zhang, Y.; Sun, H.; Tan, G.; Uher, C.; Wolverton, C.; Dravid, V. P.; Kanatzidis, M. G.; *Nature*, **2014**, *508*, 327.
    **DOI:** 10.1038/nature13184
11. Duong, A. T.; Nguyen, V. Q.; Duvjir, G.; Duong, V. T.; Kwon, S.; Song, J. Y.; Lee, J. K.; Lee, J.; E.; Park, S.; Min, T.; Lee, J.; Kim, J.; Cho, S.; *Nature Comm.*, **2016**, *7*, 13713.
    **DOI:** 10.1038/ncomms13713
12. Sun, Y.; Sun, Z.; Gao, S.; Cheng, H.; Lie, Q.; Lei, F. Wei, S.; Xie, Y.; *Adv. Energy Mater.*, **2014**, *4*, 1300611.
    **DOI:** 10.1002/aenm.201470002
13. Huang, Y.; Sutter, E.; Sadowski, J. T.; Cotlet, M.; Monti, O. L. A.; Racke, D. A.; Neupane, M. R.; Wickramaratne, D; Lake, R.; K.; Parkinson, B. A.; Sutter, P.; *ACS Nano* **2014**, *8*, 10743.
    **DOI:** 10.1021/nn504481r
14. De, D.; Manongdo, J.; See, S.; Zhang, V.; Guloy, A.; Peng, H.; *Nanotechnology*, **2013**, *24*, 025202.
    **DOI:** 10.1088/0957-4484/24/2/025202

15.  Hegde, S. S.; Kunjomana, A. G.; Chandrasekharan, K. A.; Ramesh, K.; Prashantha, M.;  *Phys. B: Condens. Matter.*, **2011**, *406*, 1143-1148.
     **DOI:** 10.1016/j.physb.2010.12.068
16.  Vaughn II, D. D.; Patel, R. J.; Hickner, M. A.;  Schaak, R. E.; *J. Am. Chem. Soc.*, **2010**, *132*, 15170.
     **DOI:** 10.1021/ja107520b
17.  Le Huang, L.; Fugen Wu, F.; Jingbo Li, J.; *J. Chem. Phys.*, **2016**, *144*, 114708.
     **DOI:** 10.1063/1.4943969
18.  Qin, G.;  Qin, Z.;  Fang, W.-Z.;  Zhang, L.-C.;  Yue, S.-Y.;  Yan, Q.-B.; Hu, M.; Su, G.; *Nanoscale*, **2016**, *8*, 11306.
     **DOI:** 10.1039/C6NR01349J
19.  Ji, Y.;  Yang, M.;  Dong, H.; Wang, L.;  Houa, T.;  Li, Y.; *J. Mater. Chem. A*, **2017**, *5*, 1734.
     **DOI:** 10.1039/C6TA08321H
20.  Zhou, Y. *J. Mater. Chem. A*, **2016**, *4*, 10906.
     **DOI:** 10.1039/C6TA03076A
21.   Kresse, G.; Hafner, J.; *Phys. Rev. B: Condens. Matter Mater. Phys.*, **1993**, *47*, 558.
     **DOI:** 10.1103/PhysRevB.47.558
22.  Kresse, G.; Furthmüller, J.; *Phys. Rev. B: Condens. Matter Mater. Phys.*, **1996**, *54*, 11169.
     **DOI:** 10.1103/PhysRevB.54.11169
23.  Kresse, G.; Joubert, D.; *Phys. Rev. B: Condens. Matter Mater. Phys.*, **1999**, *59*, 1758.
     **DOI:** 10.1103/PhysRevB.59.1758
24.  Grimme., S.; *J. Comput. Chem.*, **2006**, *27*, 1787.
     **DOI:** 10.1002/jcc.20495
25.  Krukau, A. V.; Vydrov, O. A.; Izmaylov, A. F.; Scuseria, G. E.; *J. Chem. Phys.*, **2006**, *125*, 224106.
     **DOI:** 10.1063/1.2404663
26.  Bardeen, J.; Shockley, W.; *Phys. Rev.*, **1950**, *80*, 72−80.
     **DOI:** 10.1103/PhysRev.80.72
27.  Gomes,  L. C.; Carvalho, A.; *Phys. Rev. B*, **2015**, *92*, 085406.
     **DOI:** 10.1103/PhysRevB.92.085406
28.   Li, F.; Liu, X.; Wang, Yu, Li, Y.; *J. Mater. Chem. C*, **2016**, *4*, 2155.
     **DOI:** 10.1039/C6TC00454G
29.  Huang, Y. C.; Chen, X.; Wang, C.; Peng, L.; Qian, Q.; Wang, S. F.; *Nanoscale*, **2017**, *9*, 8616.
     **DOI:** 10.1039/C7NR01952A
30.  Li, Li, Huang, L.; Snigdha, G.; P.; Yu, Y.; Cao, L.; *ACS Nano*, **2012**, *6*, 8868.
     **DOI:** 10.1021/nn303745e
31.  Shojaei, F.; Kang, H. S.; J. Phys. Chem. C., 2015, 119, 20210.
     **DOI:** 10.1021/acs.jpcc.5b07323